applied sciences

MDPI

Article

Numerical Modelling of Droplets and Beads Behavior over Super-Hydrophobic and Hydrophilic Coatings under in-Flight Icing Conditions

Giulio Croce *, Nicola Suzzi, Marco Pretto and Pietro Giannattasio

Dipartimento Politecnico di Ingegneria e Architettura, University of Udine, Via delle Scienze 206, 33100 Udine, Italy; nicola.suzzi@uniud.it (N.S.); marco.pretto@uniud.it (M.P.); pietro.giannattasio@uniud.it (P.G.)
* Correspondence: giulio.croce@uniud.it; Tel.: +39-3204365840

Featured Application: Use of hydrophobic coatings as passive inflight icing safety device.

Abstract: Current technology has produced a wide range of advanced micro-structured surfaces, designed for achieving the best wettability and adhesion performances for each specific application. In the context of in-flight icing simulations, this opens new challenges since the current most popular and successful ice accretion prediction tools neglect the details of the droplet behavior opting for a continuous film model. Here, a phenomenological model, following, in a Lagrangian approach, the evolution of the single droplets from the impinging to the onset of rivulets, is developed to simulate the performances of super-hydrophobic surfaces in icing application. Possible rebound and droplet spread on the impact, coalescence, single ice bead formation and droplet to rivulet transition are taken into account. The first validation shows how the models are able to predict the anti-icing capability of a super-hydrophobic surface coupled with a heating system.

Keywords: droplets; super hydrophobic; phenomenological model; icing; rivulets

Citation: Croce, G.; Suzzi, N.; Pretto, M.; Giannattasio, P. Numerical Modelling of Droplets and Beads Behavior over Super-Hydrophobic and Hydrophilic Coatings under in-Flight Icing Conditions. *Appl. Sci.* **2022**, *12*, 7654. https://doi.org/10.3390/app12157654

Academic Editor: Filomena Piscitelli

Received: 27 December 2021
Accepted: 25 July 2022
Published: 29 July 2022

1. Introduction

Most of the numerical models adopted in in-flight icing simulations are essentially based on the Messinger model [1] and its extension to three-dimensional arbitrary surfaces [2], combined with the prediction of impinging mass flow following either a Lagrangian or Eulerian [3] droplet flow field analysis. The runback water layer is implicitly assumed to behave as a continuous film whose velocity is mainly defined by the shear stress. In the most sophisticated form, this approach allows for full integration into a three-dimensional computational fluid dynamics (CFD) model, and offered efficient and accurate results in a number of highly complex applications, up to the analysis of a whole aircraft. However, it inherently skips most of the micro-scale effects related to the wettability and adhesion properties of the substrate, as well as the details of the transitions between moving droplets, rivulets, and full film flow regimes; actually, the smaller scale of these phenomena would require unpractically refined grids. An exception is given by roughness models developed on the basis of a droplet distribution analysis [4].

On the other hand, the advances in the development of micro- and nano-structured surfaces provide a number of highly specialized surfaces, designed either for hydrophobicity or low ice adhesion properties, that are promising as passive anti-icing tools [5–8]. Although ice phobicity and hydrophobicity are not synonyms, and their correlation is a matter of basic research [9,10], it is clear that some typical features of super-hydrophobic surfaces, such as the higher probability of impinging droplet rebound or the reduction of liquid–solid contact (and heat transfer) areas will help with an anti-icing strategy. Laboratory tests can define such micro-scale properties, usually via the analysis of a single droplet,

but the actual performance under real-world in-flight icing conditions is highly dependent on their interaction with the outer, macroscale flow field.

Thus, a kind of bridge is required to transfer the relevant micro-scale information to the macroscale analysis around a whole airfoil or a whole airplane. In particular, considering a super-hydrophobic surface, we have a few mechanisms that affect the ice accretion process. First, above a threshold impinging velocity (i.e., Weber number) and low wettability, impinging droplets may rebound, effectively reducing the collection efficiency, or (at even higher Weber) may break down into smaller droplets [11], affecting the local ice beads' related roughness and coalescence processes [12,13]. For an extremely water repellent surface, the rebound may occur at relatively low *We* [14,15], and it is worth noting that the physical phenomena behind the rebound are quite complex and might be strongly affected by the topological details of the surface roughness and its different scales [15,16]. Furthermore, the jumping droplet may stick to the surface after a few rebounds at lower energies.

As a second relevant effect, low hysteresis greatly enhances the runback water drainage, since most droplets are quickly removed, ideally preventing the formation of a continuous film. A population of droplets, either still or moving, will obviously have different active heat transfer surfaces with respect to a continuous film [17–19], as well as different equivalent runback water velocities, thus strongly affecting both the ice accretion and the evaporation process. In particular, solid–liquid and air–liquid heat transfer will occur through the droplet base circle (wet area fraction) and spherical cap surfaces, respectively, while the velocity will be defined by the balance of forces acting on the droplets.

However, if the liquid water content is high enough, the moving droplets may merge, forming individual rivulets; the rivulets, then, may coalesce forming a continuous film [20]. Even these transitions are strongly affected by the wettability properties, which in turn control the stability of the contact lines.

Here, a phenomenological approach is chosen in order to assess the performance of super-hydrophobic coatings under icing conditions. The unsteady evolution of a population of individual droplets is predicted as a function of flow conditions (median volume diameter MVD, liquid water content LWC) and surface wetting properties (contact angles, surface tension) on uniform or non-homogeneous surfaces. The simulations are performed following a Lagrangian approach, where the individual impinging droplets behave according to specified rules driving rebound, break-up, and shear-induced motion. The droplet will grow or reduce due to coalescence, evaporation or freezing.

The main aim of the work is to provide a suitable framework for an efficient evaluation of the cumulative effect of a large ensemble of droplets over a (relatively) large surface characterized by variable wettability properties and local fluid dynamic related parameters (shear stress, pressure gradients), validating the results on a typical icing example. In such cases, the full numerical modeling of all of the smaller scale effects would become prohibitive, while the phenomenological approach preserves the computational efficiency.

2. Phenomenological Model

The process of in-flight ice accretion includes several steps, each involving different physical phenomena, different scales and different regimes. The starting point is a cloud of supercooled droplets. These droplets, driven by the airflow field, impinge on the surface: the first impact location is entirely defined by the macroscopic scale droplet and airflow fields, and may be predicted via straight CFD modeling.

On the other hand, the post-impact evolution of the droplet is defined by the solid–liquid interaction features at the microscale. In particular, following [11], at low velocity, small droplet size, and high surface tension (i.e., low Weber number), the droplets stick on the surface, after a brief unsteady spreading step, assuming a roughly spherical cap shape defined by the liquid–solid contact angle. Above a threshold *We* number, they will rebound, re-emerging from the surface with a lower kinetic energy. Following the first rebound, the droplet will be driven again by the airflow drag forces, which may either move it far away from the solid surface or push it to a secondary impingement, possibly

ending as a sticking drop further downstream. Furthermore, we have the possibility of rebounding droplets interactions with new incoming ones. As noted in the introduction, the physical mechanisms inducing super-hydrophobicity are quite complex, and at extreme low wettability rebound may occur even at the lowest *We*: thus, the proposed description and modeling of the process does not pretend to be appropriate for any possible coating design (which would be a task well beyond the scope of the present work), but aims to offer a suitable tool for the analysis of the most common standard super-hydrophobic isotropic surfaces.

The actual quantity of water on the surface, in the form of a collection of spherical cap-shaped droplets, is thus a result of the initial collection efficiency, reduced by the rebounding mass flow, plus the water mass recovered from the secondary rebound and drop–drop collisions.

The droplet's evolution on the surface is driven by aerodynamic drag, pressure gradient and surface tension, as well as by the growth via coalescence with new impinging drop and mass losses via evaporation or freezing. Thus, they may remain as sticking droplets, evolving into frozen beads, or they may run along the surface as individual droplets or merge into rivulets and possibly a film.

In order to develop a complete phenomenological model, each of the above-mentioned steps and mechanisms must be described and taken into account with reasonable accuracy.

2.1. Droplet Impact Modeling

The evaluation of impinging collection efficiency requires interaction with the macro-scale flow. Here, the amount of water hitting the airfoil is evaluated in a standard way via Lagrangian tracing of droplets within a flow field computed via CFD tools (SU2 open-source code), assuming one-way coupling (droplets do not impact on the airflow field). The impact dynamics are quite complex: a comprehensive analysis and comparison may be found in [15]. Here, we follow the model of Attane et al. [13].

The droplet energy is the sum of kinetic E_K and surface energy E_σ, which in turn is the sum of the contributions from both solid–liquid S_{sl} and liquid–air S_{la} interfaces.

$$E_\sigma = S_{la}\sigma + S_{sl}\sigma(1 - cos\theta_s) \tag{1}$$

The droplet energy decreases in time due to the sum of internal viscous dissipation E_μ and the capillary rim dissipation E_μ^* [13]:

$$\frac{dE_K}{dt} + \frac{dE_\sigma}{dt} + E_\mu + E_\mu^* = 0 \tag{2}$$

The surface and kinetic energy terms, as well as the internal viscous dissipation E_μ (which include dissipation within the droplets and friction losses at the liquid–solid interface), are integrated approximating the droplet shape during the impact as a shallow cylinder of radius r and height h, while assuming an axisymmetric velocity field in the radial x and normal coordinate y:

$$u_x = \frac{2\dot{r}}{rh}xy \quad u_y = -\frac{2\dot{r}}{rh}y^2 \tag{3}$$

Figure 1 shows a sketch of the approximated geometries. In Equation (3), $\dot{r}$ is the time derivative of the base radius of the droplet, i.e., its spreading (or retracting) velocity. The rim dissipation E_μ^* is evaluated via the following correlation [13]:

$$E_\mu^* = 4.48\pi \cdot \mu \cdot r \left(\frac{Re}{\sqrt{We}}\right)^{\frac{2}{3}} \dot{r}^2 \tag{4}$$

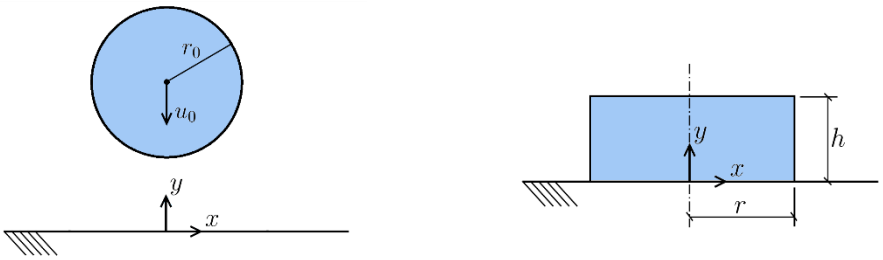

(**a**) (**b**)

Figure 1. Droplet evolution sketch, following [13], and coordinate system. (**a**) impinging droplet, (**b**) shallow cylinder approximating the droplet shape during the spreading and retreat phase.

The local droplet Weber and Reynolds numbers are defined as

$$We = \frac{\rho u_0^2 r_0}{\sigma} \tag{5}$$

$$Re = \frac{\rho u_0 r_0}{\mu} \tag{6}$$

where r_0 and u_0 are the incoming droplet radius and velocity, while σ, μ and ρ represent water surface tension, viscosity and density. Substituting in (1) we obtain an ordinary differential equation that can be solved in time. As initial conditions, we assume that both kinetic and surface energies are still equal to the incoming spherical droplet values: such conditions enable the evaluation of both the initial drop diameter and its advancing velocity. Figure 2 shows the time history of the droplet base radius r (normalized with the incoming droplet radius r_0): agreement with experimental data as in [13] is reasonably good, in particular in terms of maximum spread, while the radius oscillation time scale is over-predicted.

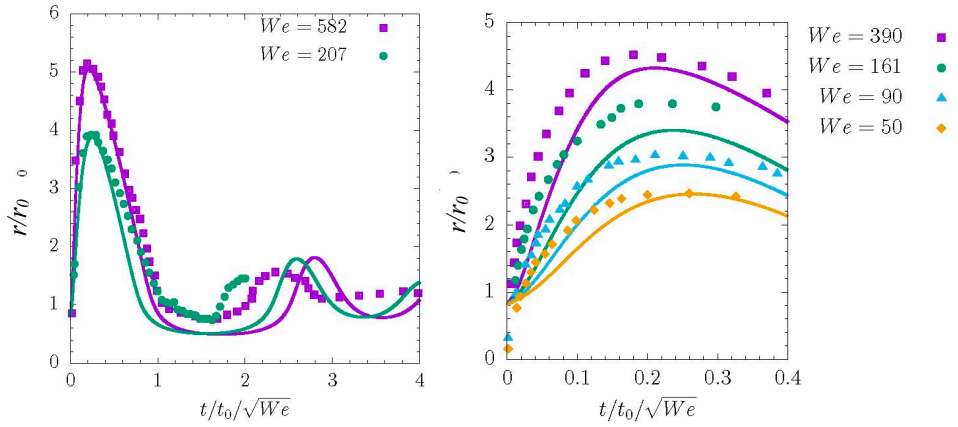

Figure 2. Droplet base radius r evolution in time: symbol: experimental data, lines: computed values. Left, $\theta_s = 87°$, $Re = 588 \cdot We^{0.5}$; right, $\theta_s = 100°$, $Re = 454 \cdot We^{0.5}$.

Time-dependent simulations at increasing *We* may be used to define a rebounding condition, which occurs when the droplet returns to its initial impact shape with residual kinetic energy. The identification of the transition to splashing is a complex problem. Different regimes (aerodynamic or hydrodynamic dominated) lead to different functional dependencies [15]. Here, for the sake of consistency, we follow the same approach used for the rebound limit: a further increase in *We* leads to a second threshold, above which the droplet radius oscillations appear overdamped and it no longer retracts down to the initial shape. This second level is assumed as the onset of corona splashing.

A computation campaign at different *We* and *Re* was performed, and from post-processing of the result the following correlations are derived for the two limiting values:

$$We_{c,r} = a\frac{(1-\cos\theta_s)^l}{log(1+Re) - b\theta_s^m} \tag{7}$$

$$We_{c,s} = c(1-\cos\theta)^n Re^2 \tag{8}$$

With a = 2.85737, b = 10.0471, l = −2.32544, m = −1.01734, c = 7.13676 × 10^{-5}, n = 6.81775. Results are shown in Figure 3, where it is evident that for any *Re* the range of *We* allowing for full rebound gets smaller and smaller at low contact angles. Results from Equation (7) can be compared with a regime map obtained from numerical fully 3D, level set approach-based results at *Re* = 800 [21]: at θ_s = 100 and 120 the transition from adhesion and rebound is located at *We* ~ 2.0 and *We* ~ 0.6, respectively, while Equation (7) offers *We* = 2.0 and *We* = 0.57. Note also that Equation (8), for a given contact angle, locates the splashing at constant product of $We_{c,s}{\cdot}Re^{-2}$, which is consistent with the experimental results in [22].

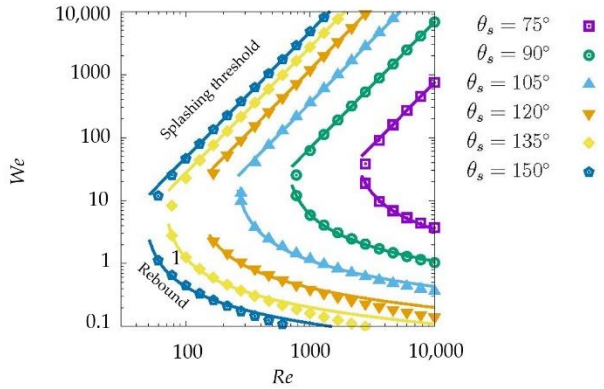

Figure 3. Rebound threshold (lower branch) and splashing threshold (upper branch) as a function of *We*, *Re* and wettability. Solid lines: correlations Equations (7) and (8). Symbols: computed values. For any given *Re* and contact angle rebound occurs if *We* falls between the two thresholds.

2.2. Collection Efficiency

The actual water mass flowing on the wall surface will be the combined result of the first impact, possible rebound, secondary impingement and, potentially, the interaction between rebounding and incoming droplets. Several CFD tools may be used at this step: here, we combine the SU2 open-source solver with an in-house Lagrangian droplet tracking code. Eulerian modeling is in general more efficient, but it is trickier to take into account the rebound and the secondary impacts on the walls and between droplets.

A population of incoming droplets is generated according to the LWD and airspeed, and their individual behavior is followed. The threshold values from the previous paragraph are used to determine whether the impinging droplet sticks on the surface or rebounds: in the latter case, the residual kinetic energy determines the speed at which the bouncing droplet leaves the surface and, thus, the subsequent droplet trajectory and its maximum height. The droplet re-emerging from the surface may be driven away from the wall, or experience a secondary impact a bit downstream. Since at any impact we have some dissipation, most droplets will then stick at a location a bit downstream of the first one. In such a case, the final position is noted and collection efficiency is evaluated by integrating over a reasonable time interval Δt. If the incoming droplet volume is V_d, and n_i is the number of droplets that came to halt on a wall element of the CFD mesh of surface ΔS, during Δt, the collection efficiency β is computed as:

$$\beta = \frac{u_0 LWC{\cdot}\Delta t{\cdot}\Delta S}{n_i{\cdot}\rho V_d} \tag{9}$$

The correlations defined in Equations (7) and (8) are extended to the case of droplets impinging at a non-zero incidence by using the normal component of the incoming velocity, as suggested in [23].

2.3. Droplet Behavior and Runback Water Modeling

Modeling the runback water flow over a hydrophobic surface requires a simulation of the evolution of the droplet population that takes properly into account the wetting properties of the surface. These phenomena involve small-scale modeling, on the size of the individual droplets, and the information required from the larger-scale flow field is limited essentially to the amount of incoming water (i.e., the collection efficiency) and its geometrical and dynamic characteristics (diameter, velocity components normal and parallel to the wall), as well as the wall shear stress and pressure gradients. A possible choice is to follow the evolution of each individual droplet after impinging via a Lagrangian approach: since the number of involved droplets is very high, a full multiphase CFD computation would quickly become unpractical. However, it is possible to simplify the process with a phenomenological model that describes the main steps of the evolution, namely impinging density, growth or reduction via coalescence and/or phase change and aerodynamic drag-induced motion. These computations will be performed over a small portion of the surface and are meant to provide, via integration, useful information in order to offer corrections to the standard, continuous film models usually assumed for icing simulation on regular surfaces.

We will assume that the droplets have a spherical cap shape, defined by their static contact angle θ_s, while the hysteresis between advancing and receding contact angles will be used in order to define the droplet's force and energy balances. Additional elements that need to be tracked are frozen beads and possibly rivulets. The former appears as spherical segments, covering the base of the droplet and progressively growing until the liquid phase disappears; the latter is modeled as an ensemble of interconnected droplets. The simulation is carried out on a two-dimensional domain, which may be representative of an arbitrarily shaped surface as long as we provide the proper distribution of shear stress, collection efficiency and pressure gradients from the CFD solution of the macro-scale problem.

The main workflow of the procedure may be summarized in the following steps:

1. Generation of N impinging sites at random locations, depending on local collection efficiency.
2. Coalescence check between new impinging droplets and existing ones.
3. Heat transfer balance for any single droplet.
4. Evaluation of freezing or evaporating mass flow.
5. Frozen mass will either contribute to the growth of an existing ice bead or create a new one at the freezing bead location.
6. Droplet stretching limit check, detecting possible rivulet onset.
7. Droplet and rivulet movement check, including coalescences along the moving path.
8. Next time step.

The procedure described above was originally developed for a high-fidelity modeling of icing roughness [4], and it has already been validated and applied to different problems [18,19,24].

A population of incoming droplets is randomly generated at each time step. As an example, on a rectangular domain $L_x \times L_y$ we define a maximum number of impinging sites at any time step as

$$N^0 = \frac{u_0 LWC \cdot \Delta t \cdot L_x \times L_y}{\rho V_d} \tag{10}$$

Then, given three random numbers $\alpha_x, \alpha_y, \alpha_c$; $0 < \alpha < 1$ the possible impinging sites $(x, y)_i$, $i = 1, N^0$ are defined as $\left(L_x \alpha_x, L_y \alpha_y\right)_i$, but they get activated only if $(\alpha_c)_i < \beta$, thus statistically complying with the computed collection efficiency.

Once an initial distribution of the impinging droplets is given, we check if any coalescence occurs. Coalescence takes place when the distance between the centers of two droplets is less than the sum of their radii, and it results in a larger drop whose volume is equal to the sum of the volumes of the parent droplets, located at the center of mass of the two parent droplets. In the case of partially frozen beads, coalescence will involve only the residual liquid volume, leaving the existing solid beads unchanged.

For hydrophilic substrates ($\theta_s < 90°$), coalescence will occur if the distance d between the centers on the surface is lower than the sum of the base area radii:

$$d \leq r_1 sin\theta_s + r_2 sin\theta_s \tag{11}$$

while under hydrophobic conditions it will occur according to the geometrical consideration in Figure 4, as

$$\sqrt{d^2 + (r_1 - r_2)^2 cos^2\theta_s} \leq r_1 + r_2 \tag{12}$$

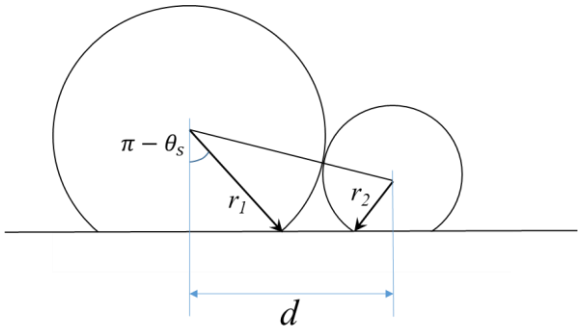

Figure 4. Coalescence condition for the hydrophobic substrate.

Droplets are subjected to external forces, namely gravity, aerodynamic drag and pressure gradient if exposed to a fluid flow. Drag is evaluated via a drag coefficient computed for spherical caps and from the local flow velocity. The local velocity, given the small height of the droplets, is computed from the local shear stress, assuming a linear profile normal distance from the wall. These forces deform the droplet shape, inducing hysteresis due to the difference between the advancing θ_a and receding θ_r contact angles. The actual contact angle will be a function of the azimuthal angle along the contact line, as reported in [25,26]. The balance of drag, gravitational force projected along the surface, and surface tension defines whether the droplet will stay still or will be shed away. Since aerodynamic drag increases with r^2, gravity contribution with r^3, and surface tension only with r, we can find a maximum radius allowing for immobile drops.

Then, the next step is the modeling of the moving droplet. A power balance between aerodynamic force work, surface tension work, and viscous dissipation (sum of laminar viscous dissipation within the droplet and wedge dissipation) is performed.

Then, the next step is the modeling of the moving droplet. Following [18,19], a power balance between aerodynamic force work, gravity force work, surface tension work and viscous dissipation (sum of laminar viscous dissipation within the droplet and wedge dissipation) is performed,

$$\Phi_D + \Phi_g - \Phi_\sigma - \Phi_\mu = 0 \tag{13}$$

$$\Phi_D = \boldsymbol{F}_D \cdot \boldsymbol{u}_d = \frac{1}{2}\rho_a c_D |\boldsymbol{u}_a - \boldsymbol{u}_d|(\boldsymbol{u}_a - \boldsymbol{u}_d) \cdot \boldsymbol{u}_d \tag{14}$$

$$\Phi_g = \boldsymbol{F}_g \cdot \boldsymbol{u}_d = \rho_l V_d \boldsymbol{g} \cdot \boldsymbol{u}_d \tag{15}$$

where $\boldsymbol{u}_a$ is the local airflow velocity and c_D is the drag coefficient, which can be estimated as the one of a flow past a sphere, as done by [27]. The further condition that the droplet moving direction agrees with the one of the resulting force $\boldsymbol{F}_g + \boldsymbol{F}_D$ is required in order to close the problem. The derivation of surface tension work Φ_σ and viscous dissipation Φ_μ

(given by the sum of laminar viscous dissipation within the droplet and wedge dissipation) are given in [18,19]. The procedure is suited for both planar and curved surfaces, provided that the substrate radius of curvature is larger than the droplet one.

2.4. Phase Change

At each time step, the energy balance of each individual droplet is performed in order to define the freezing and evaporating mass flow rates [28]:

$$q_s = q_a + m_{ev}\lambda_{ev} - m_f\lambda_f \tag{16}$$

Here, q_s is the heating flux from the solid wall, if present, and q_a is the convective heat transfer computed using the local heat transfer from the macroscale computation and the actual droplet surface exposed to the air, while evaporating mass flow m_{ev} comes from a heat and mass transfer analogy, m_f is the freezing mass and λ_{ev}, λ_f the evaporation and fusion of latent heat.

2.5. Rivulet Onset

At high wettability, or for high impinging mass flow, and low freezing rate, we can have a runback water mass flow so high that the individual droplet regimes may give way to the onset of rivulets. Here, a rivulet threshold is obtained via a force balance over half of the droplet, as suggested in [20]. Essentially, we cut the droplet with a midspan plane, normal to the drop velocity and to the substrate (Figure 5). If the resultant R of the forces (due to drag, gravity, surface tension along the contact line, viscous force on the wet area) over half of the droplet (assumed symmetric) is larger than the surface tension action $F_{\sigma i}$ along the wet perimeter on the plane cut, we can assume that the droplet is starting to stretch and is evolving into a rivulet.

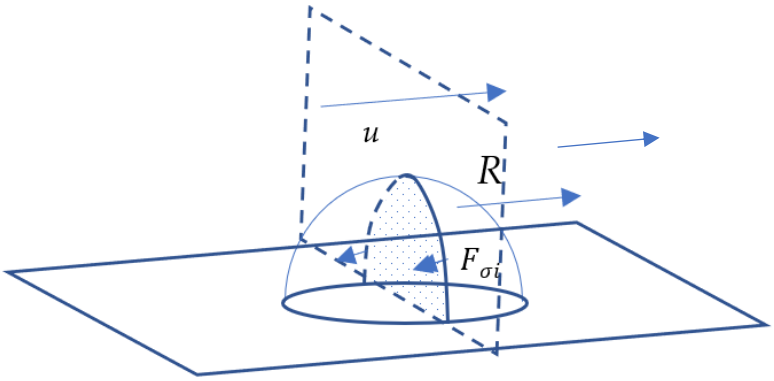

Figure 5. Sketch of the droplet stability balance.

Once the rivulet has started, it will move downstream driven by the sheart stress. At high wettability, or for high impinging mass flow, and low freezing rate, we can have a high runback water mass flow so high that the individual droplet regimes may give way to the onset of the rivulet. Once the rivulet is generated, it is modeled as a series of interconnected circles, in order to easily allow for coalescence check with the existing droplets according to Equations (11) and (12). In Figure 6, the typical evolution is shown: to the left, a large droplet is running from the bottom to the top until the growth due to the coalescence with the other drops along its trajectory triggers the rivulet transition. From this point, the rivulet height is fixed, and the possible increase in mass flow due to coalescences results in its widening. Furthermore, we assume a triangular velocity profile normal to the wall aligned with the shear as in the usual continuum model based on Messinger's approach.

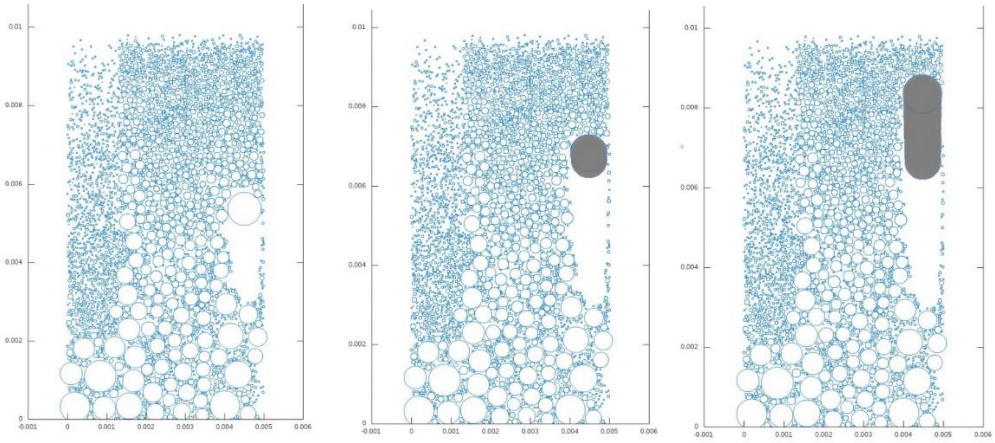

Figure 6. Droplet−rivulet transition, droplet distribution at three different time steps. From left to right: individual droplet running downstream, rivulet onset (grey area), rivulet development.

3. Results

For a first assessment of the capability of the procedure outlined above, the experimental setup of [29] was simulated. A small-scale NACA0012 profile is considered, with a chord of 150 mm, partially heated and coated with combinations of hydrophobic and hydrophilic sections.

In particular, we considered a case with a freestream velocity of 40 m/s, freestream temperature of −5 °C, LWC = 1.0 g/m^3, and droplet size of 30 µm. The airfoil is heated for 5% of the chord length, with a heat flux of 33 W along the 400 mm spanwise length. We compare two cases: in the first, the heated region is hydrophilic ($\theta_s = 65°$, $\theta_a = 105°$, $\theta_r = 50°$) and the remaining area super-hydrophobic ($\theta_s = 157°$, $\theta_a = 159°$, $\theta_r = 154°$), in the second case the whole surface is super-hydrophobic.

Figure 7 shows the collection efficiency, taking into account rebound and secondary impacts for both cases. The effect is quite dramatic, with a nearly clean leading edge region, although it is important to note that the very small thickness of the airfoil maximizes the effect of rebound. The droplets with higher *We* will rebound around the leading edge, and due to the small thickness of the airfoil, only a small fraction of them stops on the solid wall after a few secondary impacts. However, these droplets landing somewhat downstream with respect to their first impact are responsible for the recovery at $x = 0.01$, where the collection efficiency is even higher than that in the hydrophilic region.

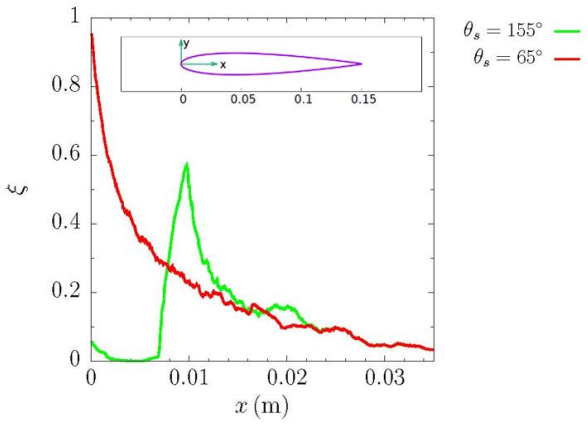

Figure 7. Resulting collection efficiency, taking into account super-hydrophobic surface rebound.

The effect of the reduction in water gathering, combined with the improved drainage of the smaller, low hysteresis droplets on the super-hydrophobic surface, leads to a better performance of the fully hydrophobic airfoil. In particular, the droplet evolution was computed on a small strip near the leading edge, as shown in Figure 8. Two snapshots

of the droplet population are presented: red circles refer to liquid droplets and blue ones to frozen beads. It is clear that we have better drainage in the hydrophobic setup, with smaller and quicker droplets that evaporate or run downstream before any freezing. On the other hand, the hydrophilic leading edge generates larger droplets and slower flow, and thus we still have runback water beyond the heated strips, allowing for ice accretion as observed in the experiment.

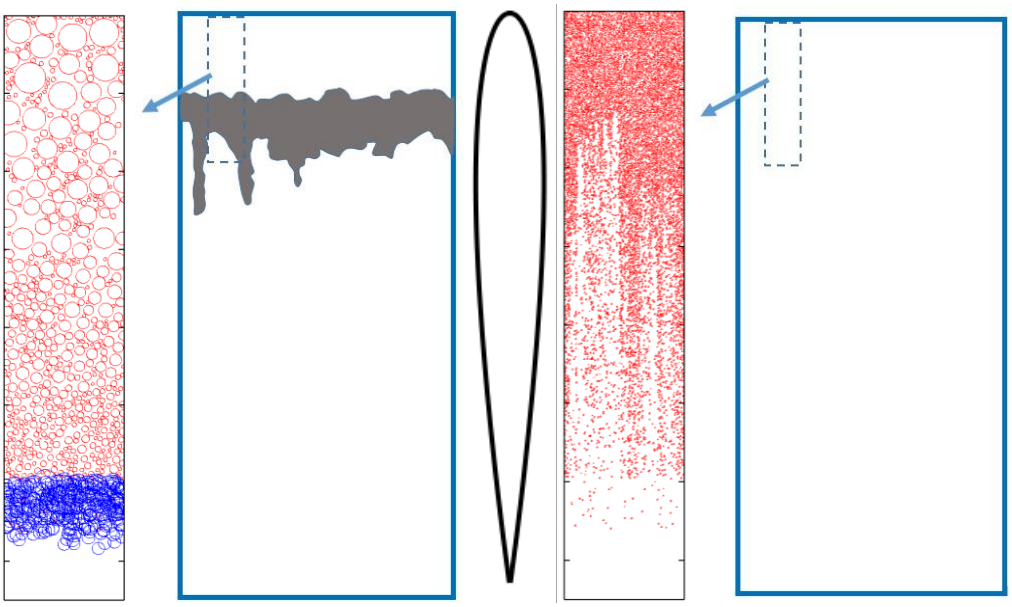

Figure 8. Computed results: red, liquid droplets. Blue, frozen beads. Experimental data, reconstructed from [29]: dark grey: iced area. Left, hydrophilic leading edge on an otherwise hydrophobic coated airfoil. Right, fully hydrophobic coated airfoil.

Interactions between rebounding and incoming droplets are, on the contrary, nearly negligible: Figure 9 shows the computed collision density, i.e., the number of collisions between rebounding and incoming droplets per unit time and volume, around the airfoil profile. The maximum value is attained in the region of the secondary peak in the collection efficiency, at $x \sim 10$ mm, and is a bit less than 140 $s^{-1} \cdot m^{-2}$, i.e., it is several orders of magnitude lower than the number of the actual flying droplets at the same location.

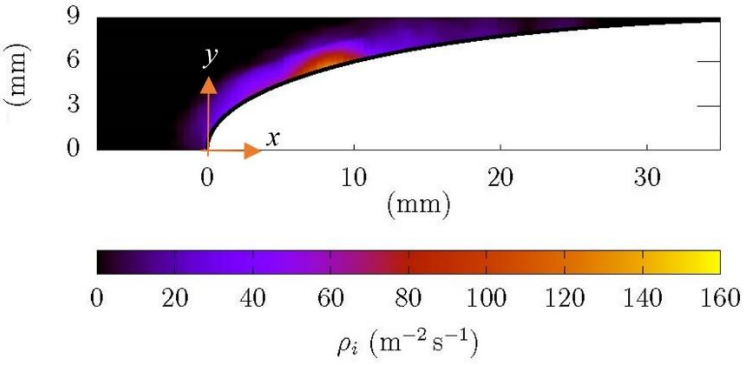

Figure 9. Collision density between rebounding and incoming droplets on NACA 0012 profile, super-hydrophobic surface.

4. Conclusions

A comprehensive workflow, designed to simulate the effects of hydrophobic coatings under icing conditions, was described. The aim was to offer the possibility to estimate the impact of wettability properties in an efficient way, using a phenomenological model that

takes advantage of several models either readily available in the literature or adapted for the specific application.

A number of different effects, however, had to be taken into account, involving different scales: droplet rebound, rivulet formation, and droplet–droplet interactions. The first validation case offers only a threshold-like comparison, which allows verifying that protection from ice formation is predicted. Thus, further detailed analysis and validation of the individual mechanisms are still required: due to the complexity of the physical phenomena and to the variability of the design of super super-hydrophobic coatings, the models and phenomenological rules, in particular those related to the bouncing/splashing, proposed in the present work, do not pretend to cover all of the possible regimes and surfaces topology beyond those used in the validation cases. However, these first results demonstrate that via the proposed computational framework it is actually possible to predict the beneficial effect of properly designed coatings for ice mitigation purposes in a real-world application.

Author Contributions: Writing—original draft, G.C.and N.S.; Writing—review & editing, M.P. and P.G. All authors have read and agreed to the published version of the manuscript.

Funding: The present work was funded by the EU, within IMPACT project, call JTI-CS2-2019-CfP10-LPA-01-80, Clean Sky 2 Joint Undertaking (JU) under grant agreement No. 885052.

Data Availability Statement: Validation data come from quoted open literature.

Conflicts of Interest: The authors declare no conflict of interest.

Nomenclature

h	droplet height
E_σ	surface energy
E_K	kinetic energy
E_μ	viscous dissipation
E_μ^*	rim dissipation
$\boldsymbol{F}_D$	drag force
$\boldsymbol{F}_g$	gravity force
$\boldsymbol{F}_\sigma$	rigidity force
g	gravity acceleration
$\dot{m}_{ev}$	evaporating mass flow rate
$\dot{m}_f$	freezing mass flow rate
N^0	number of impinging sites
q	heat flux
r	droplet radius
Re	droplet Reynolds number, $\rho ur/\mu$
S_{la}	liquid–air interface area
S_{sl}	solid–liquid interface area
t	time
$\boldsymbol{u}_a$	air velocity
$\boldsymbol{u}_d$	droplet velocity
V_d	droplet volume
We	droplet Weber number, $\rho u^2 r/\sigma$
x, y	Cartesian coordinates
β	collection efficiency
θ_s	static contact angle
λ_{ev}	evaporation latent heat
λ_f	fusion latent heat
μ	dynamic viscosity
ρ	Density

σ	surface tension
Φ_D	drag force work
Φ_g	gravity force work
Φ_σ	surface tension work
Φ_μ	viscous dissipation

References

1. Messinger, B.L. Equilibrium Temperature of an Unheated Icing Surface as a Function of Air Speed. *J. Aeronaut. Sci.* **1953**, *20*, 29–42. [CrossRef]
2. Bourgault, Y.; Beaugendre, H.; Habashi, W. Development of a shallow-water icing model in FENSAP-ICE. *J. Aircr.* **2000**, *37*, 640–646. [CrossRef]
3. Bourgault, Y.; Boutanios, Z.; Habashi, W.G. Three-dimensional Eulerian approach to droplet impingement simulation using FENSAP-ICE, Part 1: Model, algorithm, and validation. *J. Aircr.* **2000**, *37*, 95–103. [CrossRef]
4. Croce, G.; De Candido, E.; Habashi, W.G.; Munzar, J.; Aubé, M.S.; Baruzzi, G.S.; Aliaga, C. FENSAP-ICE: Analytical model for spatial and temporal evolution of in-flight icing roughness. *J. Aircr.* **2010**, *47*, 1283–1289. [CrossRef]
5. Villeneuve, E.; Brassard, J.-D.; Volat, C. Effect of various surface coatings on de-icing/anti-icing fluids aerodynamic and endurance time performances. *Aerospace* **2019**, *6*, 114. [CrossRef]
6. Rose, J.B.R.; Hamilton, J.A.J.L. Experimental investigation on the alternate coating method for aircraft anti-icing applications. *IMechE J. Aerosp. Eng.* **2017**, *231*, 407–418. [CrossRef]
7. Zheng, S.; Li, C.; Fu, Q.; Hu, W.; Xiang, T.; Wang, Q.; Du, M.; Liu, X.; Chen, Z. Development of stable superhydrophobic coatings on aluminum surface for corrosion-resistant, self-cleaning, and anti-icing applications. *Mater. Des.* **2016**, *93*, 261–270. [CrossRef]
8. Tarquini, S.; Antonini, C.; Amirfazli, A.; Marengo, M.; Palacios, J. Investigation of ice shedding properties of superhydrophobic coatings on helicopter blades. *Cold Reg. Sci. Technol.* **2014**, *100*, 50–58. [CrossRef]
9. Esmeryan, K.D. From Extremely Water-Repellent Coatings to Passive Icing Protection-Principles, Limitations and Innovative Application Aspects. *Coatings* **2020**, *10*, 66. [CrossRef]
10. He, Z.; Zhuo, Y.; Zhang, Z.; He, J. Design of Icephobic Surfaces by Lowering Ice Adhesion Strength: A Mini Review. *Coatings* **2021**, *11*, 1343. [CrossRef]
11. Rioboo, R.; Voué, M.; Vaillant, A.; De Coninck, J. Drop Impact on Porous Superhydrophobic Polymer Surfaces. *Langmuir* **2008**, *24*, 14074–14077. [CrossRef] [PubMed]
12. Mao, T.; Kuhn, D.C.S.; Tran, H. Spread and Rebound of Liquid Droplets upon Impact on Flat Surfaces. *AIChE J.* **1997**, *43*, 2169–2179. [CrossRef]
13. Attané, P.; Girard, F.; Morin, V. An energy balance approach of the dynamics of drop impact on a solid surface. *Phys. Fluids* **2007**, *19*, 012101. [CrossRef]
14. Esmeryan, K.D.; Bressler, A.S.; Castano, C.E.; Fergusson, C.P.; Mohammadi, R. Rational strategy for the atmospheric icing prevention based on chemically functionalized carbon soot coatings. *Appl. Surf. Sci.* **2016**, *390*, 452–460. [CrossRef]
15. Marengo, M.; Antonini, C.; Roisman, I.V.; Trope, C. Drop collisions with simple and complex surfaces. *Curr. Opin. Colloid Interface Sci.* **2011**, *16*, 292–302. [CrossRef]
16. Bird, J.C.; Dhiman, R.; Kwon, H.; Varanasi, K.K. Reducing the contact time of a bouncing drop. *Nature* **2013**, *503*, 385–388. [CrossRef] [PubMed]
17. Qi, W.; Weisensee, P.B. Dynamic wetting and heat transfer during droplet impact on bi-phobic wettability patterned surfaces. *Phys. Fluids* **2020**, *32*, 067110. [CrossRef]
18. Croce, G.; Suzzi, N.; D'Agaro, P. Numerical prediction of dropwise condensation performances on hybrid hydrophobic-hydrophilic surfaces. *J. Phys. Conf. Ser.* **2020**, *1599*, 012006. [CrossRef]
19. De Candido, E.; Croce, G.; D'Agaro, P. Droplet Buildup and Water Retention Prediction in Condensation Processes. *Heat Transf. Eng.* **2012**, *33*, 1130–1137. [CrossRef]
20. Wang, F.; Cheng, X. Modeling approach of flowing condensate coverage rate on inclined wall for aerosol wash down. *Nucl. Eng. Des.* **2019**, *355*, 110349. [CrossRef]
21. Caviezel, D.; Narayanan, C.; Lakehal, D. Adherence and bouncing of liquid droplets impacting on dry surfaces. *Microfluid. Nanofluidics* **2008**, *5*, 469–478. [CrossRef]
22. Burzynski, D.A.; Roisman, I.V.; Bansmer, S.E. On the splashing of high-speed drops impacting a dry surface. *J. Fluid Mech.* **2020**, *892*, A2. [CrossRef]
23. Sikalo, S.; Trope, C.; Ganic, E.N. Impact of droplets onto inclined surfaces. *J. Colloid Interface Sci.* **2005**, *286*, 661–669. [CrossRef]
24. Croce, G.; D'Agaro, P.; Suzzi, N. *Optimization of Hybrid Hydrophilic-Hydrophobic Surfaces for Dropwise Condensation Enhancement*; ASME Paper ICNMM2019-4291; ASME: New York, NY, USA, 2019.
25. El Sherbini, A.I.; Jacobi, A.M. Liquid Drops on Vertical and Inclined Surfaces I. An Experimental Study of Drop Geometry. *J. Colloid Interface Sci.* **2004**, *273*, 556–565. [CrossRef]
26. El Sherbini, A.I.; Jacobi, A.M. Liquid Drops on Vertical and Inclined Surfaces II. A Method for Approximating Drop Shapes. *J. Colloid Interface Sci.* **2004**, *273*, 566–575. [CrossRef]

27. Tancon, M.; Parin, R.; Martucci, A.; Bortolin, S.; Del Col, D. Effect of steam velocity during dropwise condensation. *Int. J. Heat Mass Transf.* **2021**, *165*, 120624. [CrossRef]
28. Croce, G.; D'Agaro, P.; Della Mora, F. Numerical simulation of glass fogging and defogging. *Int. J. Comput. Fluid Dyn.* **2007**, *19*, 437–445. [CrossRef]
29. Hu, H.; Hu, H.; Liu, Y. *An Explorative Study to Use Super-Hydrophilic/Super-Hydrophobic Hybrid Surfaces for Aircraft Icing Mitigation*; SAE Technical Paper 2019-01-1995; SAE International: Warrendale, PA, USA, 2019. [CrossRef]